Journal of Applied Fluid Mechanics, Vol. 18, No. 11, pp. 2823-2836, 2025.
Available online at www.jafmonline.net, ISSN 1735-3572, EISSN 1735-3645.
https://doi.org/10.47176/jafm.18.11.3449

Study on Prediction and Optimization of Long-range Water Mist Projection

H. Z. Sun[1], X. L. Zhu[1], Z. G. Wang[2], J. Y. Zhao[1], S. Hu[1], C. H. Xu[3] and X. S. Wang[1†]

[1] *State Key Laboratory of Fire Science, University of Science and Technology of China, Hefei, 230026, China*
[2] *Nari Yihe Enviromental Technology Co., Ltd, SGCC, Beijing, 100080, China*
[3] *School of Safety Science and Emergency Management, Wuhan University of Technology, Wuhan 430070, China*

†*Corresponding Author Email: wxs@mail.ustc.edu.cn*

ABSTRACT

The development of a long-distance water mist projection device is essential for mitigating emergencies like fires, explosions, chemical leaks, and dust contamination. Currently, there is a lack of theory to predict the spray range under the effect of fan operating parameters and duct structures, which results in the blindness of long-distance water mist projection device design. By integrating fluid dynamics theory, classical jet theory, and real operational data, a semi-empirical model is developed to predict the jet range and analyze the velocity distribution of the projection device. This model can be used to identify the key factors affecting characteristics of multiphase jet and optimize the alignment between the fan and air duct. Subsequently, a long-distance water mist projection device was manufactured and tested. At a range of 30.2 m, a large-scale transformer fire with a heat release rate between 81.31 and 124.56 MW was extinguished within 3 min using the proposed device. This comprehensive study may aid the development of long-distance axial airflow-inducing water mist devices and their applications in emergency response scenarios.

Article History

Received February 17, 2025
Revised May 6, 2025
Accepted June 8, 2025
Available online September 3, 2025

Keywords:

Fire suppression
Jet range
Long-range projection
Multiphase jet
Water mist

1. INTRODUCTION

Fire, explosion, hazardous chemicals leakage, dust contamination, and other related incidents tend to rapidly escalate, leading to numerous casualties, severe environmental pollution, and substantial economic damages. For instance, the fire that broke out at Tianjin Port in China on August 12, 2015, claimed the lives of 165 individuals (including 99 firefighters), left 8 persons missing, caused injuries to 789 people, and resulted in a direct economic loss of 6,866 million RMB (Xinhua News Agency, 2015). Similarly, on August 4, 2020, a series of explosions caused by the spontaneous combustion of flammable chemicals at the port of Beirut, the capital of Lebanon, led to the deaths of at least 190 individuals (including 10 rescuers), injuries to over 6,500 people, and economic losses exceeding $15 billion (Haiwainet, 2020).

When dealing with extensive disaster areas, the most commonly employed methods for extinguishing fires from a distance in rescue operations have been the use of water cannons. However, traditional water columns have limitations in effectively suppressing explosions and eliminating pollutants. Furthermore, the high impact force of the water column can cause splashing of liquid chemicals. Water mist and multi-component water mist, on the other hand, possess a large surface area, enabling them to extinguish fires (Mawhinney et al., 1994; Jenft et al., 2014; Santangelo et al., 2014; Liu et al., 2019; Lv et al., 2019; Abdulrahman et al., 2021), efficiently adsorb pollutants, and suppress explosions (Collin et al., 2007; Gieras, 2008; Cao et al., 2017; Xu et al., 2017; Li et al., 2021; Wang, 2019). Nevertheless, the traditional water mist systems suffer from low water flow rates and limited spray range (FM Approvals, 2016); Santangelo et al., 2016; Wang, 2019), rendering them inadequate for addressing large-scale fires and explosions from afar. A previous study demonstrated that even at a water pressure as high as 10 MPa, traditional water mist systems were ineffective in extinguishing fires beyond 7.49 m from the nozzles (Santangelo et al., 2016).

In an attempt to enhance the spray range of water droplets, some researchers have explored using turbojet engines as a power source (Luo & Li, 2013; Wesierski, 2023). While this approach did achieve long-range spraying capabilities (20–70 m) and high water flow rates (up to 30 kg/s), it faced limited adoption due to challenges such as high fuel consumption (exceeding 4,000 L/h), noisy operation (over 130 dB), high airflow temperatures (above 450°C), and high costs (Zhu et al., 2022). As a more cost-effective and viable solution, high-performance electronic fans have emerged as an alternative to turbojet engines. Water mist projection devices equipped with fans have already found applications in various fields like dust

NOMENCLATURE

a	outlet turbulence coefficient
B (B_{us}, B_{ul})	bias error, subscript "*us*" denotes small scale, and "*ul*" denotes large scale.
$b_{1/2}$	half width of the jet
D	outlet diameter of the air duct, m
K	experimental coefficient
L	length of the air duct
L_1	length of rectifier section
L_2	length of straight duct
n	the number of measuring points
P_v	outlet dynamic pressure
ΔP_{loss}	static pressure loss of the air duct
Q	outlet flow rate
Re_D	outlet Reynolds number of the air duct
S (S_{us}, S_{ul})	precision error, subscript "*us*" denotes small scale, and "*ul*" denotes large scale.
s	defined jet range
U (U_{us}, U_{ul})	uncertainty, subscript "*us*" denotes small scale, and "*ul*" denotes large scale.
u_0	average velocity at the duct outlet
u_m	velocity at a distance '*x*' from the outlet section along the axis
v_i	actual velocity of each point
$\bar{v}$	average velocity of the section
W_a	fan output power
X (X_k, $\bar{X}$)	experimental measurements, subscript *k* denotes the *k*th data point, and an overline indicates an average value.
x	distance from a point on the jet axis to the jet outlet section

Greek symbols

α	jet diffusion angle
ε	roughness of inner wall of the air duct
δ	viscous sublayer thickness
λ	Darcy's friction factor of the duct
ρ	air density
η_0	internal efficiency
η_1	mechanical efficiency
ξ_0	local loss coefficient of the duct
γ_v	uniformity index

removal, agricultural irrigation, and fire extinguishing (Wang et al., 2016). Despite the applicability of classical jet theory in predicting ideal jet flow velocity characteristics, the actual structural design and operational parameters of these devices have not been optimal. The flow dynamics of air-mist multiphase flow are even more intricate, and the mechanical energy provided by existing devices is underutilized in extending the projection range of water mist. Hence, there is an urgent need to develop a more robust theoretical model to optimize long-range water mist projection devices.

When analyzing the flow field and performance of wind turbines, researchers primarily utilize numerical simulation (Li et al., 2014; Ye et al., 2017; Zhang et al., 2023) and experimental methods (Chen et al., 2000; Fernandez et al., 2007, 2011). While numerical simulation can provide detailed location data in the flow field, it often substantially deviates from the actual results. In contrast, experimental methods can offer more accurate data and provide a more intuitive understanding (Panchapakesan and Lumley, 1993; Hussein et al., 1994; Del Taglia et al., 2004; Lakehal et al., 2025). To ensure better comparison and validation with theoretical analysis, it is advisable to use experimental validation methods.

To address the aforementioned challenges, this paper aims to establish theoretical equations for analyzing the key factors influencing spray range and offer tailored solutions for fans and air ducts. Both small-scale and full-scale experiments will be conducted to investigate the air velocity field and validate the accuracy of our equations. In line with our theoretical framework, a full-scale water mist projection device will be fabricated. Subsequent full-scale experiments will be conducted to confirm the water mist projection range, water mist characteristics at the target area, and the practical effectiveness of fire suppression.

2. THEORETICAL ANALYSIS

2.1 Theoretical Model of the Air Jet Range

The complexity of axial-flow-induced spray jets means their range is influenced by various factors, including nozzle characteristics, number, position, angle, and gas-to-liquid ratio. Establishing a theoretical framework for two-phase axial-flow-induced spray jets poses substantial challenges. These factors complicate the derivation of a unified empirical model because their quantitative relationships are still poorly understood. Therefore, we propose a simplified solution by treating the spray as a source of well-following particles that move within the free jet generated by the fan. In this case, the range of the fan-induced free jet can largely describe the range of the axial-flow-induced spray jet. Consequently, developing an effective model for the range of fan-induced free jets is crucial.

The airflow structure of the projection device is illustrated in Fig. 1. For simplify the theoretical analysis, we assume that the air duct of the projection device is cylindrical. The airflow can be separated into two distinct parts. Within the duct, the airflow behaves according to the flow principles in a cylindrical pipe. Beyond the duct outlet, the airflow follows the characteristics of free submerged jet flow. The circular free jet can be further divided into three regions: initial, transition, and main regions (Abramovich, 1963; Hotz et al., 2021).

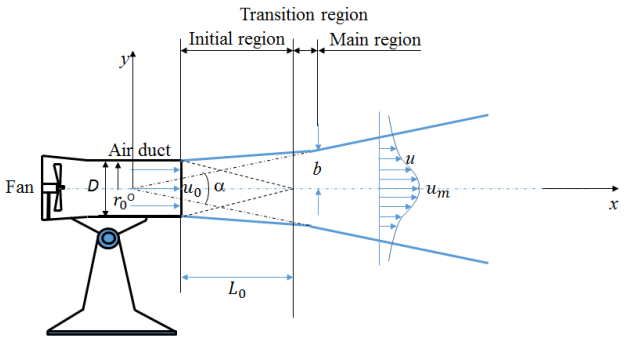

Fig. 1 Flow structure in the duct and downstream of the jet outlet

Table 1 Axial velocity decay law in the main region of free turbulent jets

Source	**Jet characteristic half thickness '*b*'**	**Jet axial velocity**
Tollmien (1926)	$b_{1/2}$=0.082 x	$\frac{u_m}{u_0}=\frac{7.32}{x/d}$
Gortler (1942)	$b_{1/2}$=0.098 x	$\frac{u_m}{u_0}=\frac{5.75}{x/d}$
Albertson (1950)	b_e=0.114 x	$\frac{u_m}{u_0}=\frac{6.20}{x/d}$
Rajaratnam & Subramanya (1967)	$b_{1/2}$=0.100 x	$\frac{u_m}{u_0}=\frac{6.30}{x/d}$

In the initial region, the central velocity of the jet maintains its initial velocity from the section, extending over a length approximately six times the nozzle diameter. Subsequently, in the transition region, the axial velocity of the jet starts to undergo a shift. Finally, in the main region, the axial velocity of the jet gradually decreases (Wu & Wang, 2021).

Building on this foundation, the jet characteristics under the coupling effect of single-phase free jet flow and duct structure can be reasoned as follows. Between the inlet and outlet of the air duct, the output power of the fan (W_a) can be expressed as (Liu et al., 2021):

$$\begin{aligned} W_a &= Q\times\left(\Delta P_{loss}+P_v\right) \\ &= \frac{\pi D^2}{4}\times u_0\times\left(\frac{1}{2}\frac{L}{D}\lambda\rho {u_0}^2+\frac{1}{2}\xi_0\rho {u_0}^2+\frac{1}{2}\rho {u_0}^2\right) \\ &= \frac{\pi D^2\rho {u_0}^3}{8}\left(\frac{L}{D}\lambda+\xi_0+1\right) \end{aligned} \tag{1}$$

where, Q is the outlet flow rate, ΔP_{loss} is the static pressure loss of the air duct, P_v is the outlet dynamic pressure.

After transformation of Eq. (1), the outlet average velocity of the fan can be expressed as:

$$u_0=\left(\frac{8W_a}{\rho\pi D\left(L\lambda+\xi_0 D+D\right)}\right)^{1/3} \tag{2}$$

Given that the airflow downstream of the duct follows the free submerged jet flow characteristics, researchers have developed empirical models to forecast the velocity distribution along the jet axis (Table 1). The models in Table 1 were constructed assuming a uniform velocity distribution at the jet outlet, although actual airflow generated by a fan is typically non-uniform. Hence, we have opted to utilize the empirical model proposed by Abramovich (Eq. (3) (1963) to describe the axial velocity distribution of the air jet. This particular model accounts for the non-uniform initial velocity distribution.

$$\frac{u_m}{u_0}=\frac{0.48}{\mathrm{a}\,x/D+0.147} \tag{3}$$

where, a is the turbulence coefficient, which depends on the turbulence degree of the fluid in the outlet section and the uniformity of the velocity distribution. The velocity at a distance 'x' from the outlet section along the axis is represented as 'u_m'.

By combining Eq. (2) and (3), the velocity distribution of the central axis can be obtained:

$$u_m=\frac{0.48}{\mathrm{a}\,x/D+0.147}\times\left(\frac{8W_a}{\rho\pi D\left(L\lambda+\xi_0 D+D\right)}\right)^{1/3} \tag{4}$$

Transforming Eq. (4), the axial distance x can be expressed as a function of the axial velocity:

$$x=\frac{D}{\mathrm{a}}\left(\frac{0.48}{u_m}\times\left(\frac{8W_a}{\rho\pi D\left(L\lambda+\xi_0 D+D\right)}\right)^{1/3}-0.147\right) \tag{5}$$

According to Plant protection machinery-general test method (2014), u_m=2 m/s is regarded as the end of the jet,

Table 2 Empirical formulas for Darcy friction factor and its scope of application

Models	Darcy friction factor	Scope of application	Flow region
Laminar flow analytical solution	$\lambda=\frac{64}{Re}$	Re<2300	Laminar flow region
Blasius formula	$\lambda=\frac{0.3164}{Re^{0.25}}$	4000<Re<10^5	Smooth region
Prandtl-Schlichting formula	$\frac{1}{\sqrt{\lambda}}$=2.0lg(Re$\sqrt{\lambda}$)-0.8	3000<Re<4×10^6	Smooth region
Kármán formula	$\lambda=\frac{1}{(1.74+2lg(\frac{d}{2\varepsilon}))^2}$	Re>4160$(\frac{d}{2\varepsilon})^{0.85}$	Fully rough region
(Colebrook, 1939) formula	$\frac{1}{\sqrt{\lambda}}$=-2.0lg$(\frac{2.51}{Re\sqrt{\lambda}}+\frac{\varepsilon/d}{3.7})$	4000<Re<10^8	Transition rough region

thus the jet range s can be finally expressed as:

$$s=\frac{D}{\mathrm{a}}\left(0.24\times\left(\frac{8W_{\mathrm{a}}}{\rho\pi D\left(L\lambda+\xi_0 D+D\right)}\right)^{1/3}-0.147\right) \tag{6}$$

Based on the Eq. (1) to (6), when the fan power remains constant, the range of the jet is influenced by factors such as Darcy's friction factor λ, turbulence coefficient " a ", and the geometry of the duct (D and L). Each of these factors will be individually analyzed in the subsequent sections.

2.2 Effect of Darcy Friction Factor

Darcy friction factor λ represents the resistance coefficient along the duct, and its value is contingent upon the Reynolds number and wall roughness. It is evident that a smaller Darcy friction factor corresponds to lower resistance and, consequently, a lengthier jet range. In laminar flow conditions, the Darcy friction factor has a theoretical analytical solution. However, in turbulent flow, it is determined by the Reynolds number, viscous sublayer thickness, and absolute wall roughness. The viscous sublayer thickness δ can be calculated using Eq. (7) (Schlichting, 1960; Daugherty et al., 1985;).

$$\delta=\frac{34.2D}{\mathrm{Re}_D^{0.875}} \tag{7}$$

In Eq. (7), D represents the diameter of the circular pipe. When the viscous sublayer thickness exceeds the absolute roughness of the wall, the pipe wall protrusion is submerged within the viscous sublayer. Experimental observations suggested that wall roughness has no impact on the Darcy friction factor in this scenario, indicating a smooth flow regime. However, if the viscous sublayer thickness is less than the wall roughness, the flow transitions into the rough region. Here, the pipe wall protrusion extends beyond the viscous sublayer, entering the turbulent transition zone or core zone, leading to turbulence interference and energy loss. Empirical formulas for the Darcy friction factor in different regions are listed in Table 2 (Daugherty et al., 1985).

Considering the aforementioned conditions, Moody (1944) developed a comprehensive λ-Re (ε/d) chart known as the Moody diagram. In engineering applications, once the Reynolds number and equivalent roughness are computed, engineers can readily determine the Darcy friction factor using the Moody diagram.

2.3 Effect of Turbulence Coefficient

The turbulence coefficient (a) is a defining factor that describes the jet structure, based on the fluid's turbulence and the uniformity of velocity distribution. Greater turbulence at the jet outlet cross-section leads to a higher turbulence coefficient, reflecting a more uneven outlet velocity distribution. Bressler et al. (1996) and Welten et al. (1993) proposed the following Eq. to quantify the uniformity of velocity distribution:

$$\gamma_v=1-\frac{1}{2n}\sum_{i=1}^{n}\frac{\sqrt{\left(v_i-\bar{v}\right)^2}}{\bar{v}} \tag{8}$$

The uniformity index, denoted as γ_v and ranging between 0 and 1, signifies the uniformity of flow. A value closer to one indicates a more uniform flow, with one representing ideal uniform flow and zero suggesting airflow passing solely through a single pipe. n is the number of measuring points. The parameter n denotes the number of measuring points. Despite its importance, no empirical model currently exists to characterize the relationship between the exit turbulence coefficient, turbulence intensity, and the uniformity of the exit velocity distribution. The turbulence coefficient must be determined experimentally. Table 3 provides a compilation of experimental data on turbulence coefficients at pipeline outlets from previous studies (Baturin & Liu, 1965).

Higher a amplifies shear layer instabilities, accelerating the transition to turbulence and increasing the jet spreading angle. Eq. 9 describes the relationship between the exit turbulence coefficient and jet diffusion angle:

$$tg\left(\frac{\alpha}{2}\right)=K\,\mathrm{a} \tag{9}$$

where, K is the experimental coefficient, α is the jet diffusion angle, and a is the turbulence coefficient. K = 6.1 for axisymmetric jets (Ministry of Machinery Industry, Fourth Academy, 1976).

Table 3 Experimental turbulence coefficient values at partial pipe outlets

Nozzle type	*a*	2α
Nozzle with a converging outlet	0.066 0.071	25°20′ 27°10′
Cylindrical tube	0.076 0.08	29°00′
Circular nozzle with guide vanes or fences	0.09	34°00′
Square nozzle	0.10	37°36′
Axial fan with air guide plate	0.12	44°30′
Axial fan with metal mesh	0.24	78°40′
Flat nozzle with excellent contraction	0.108	29°30′
Right-angle bend pipe with guide plate	0.20	68°30′
Sharp edge slit in planar wall	0.118	32°10′
Longitudinal slot on the air duct with guide vanes and rounded edges	0.155	41°20′

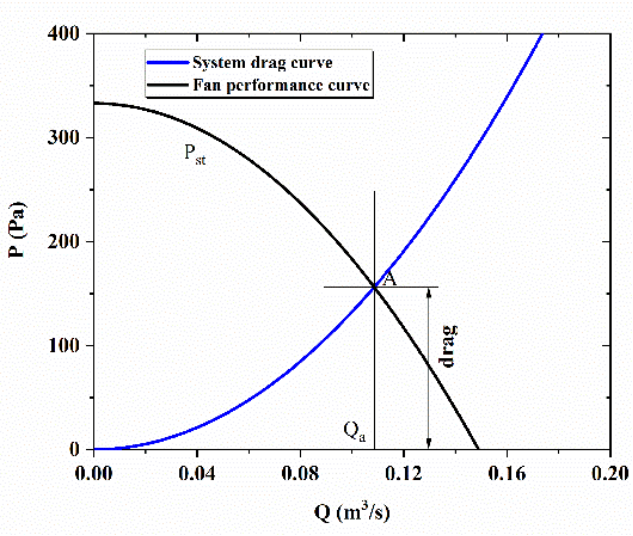

Fig. 2 Fan P-Q curve and system resistance curve

The influence of the exit turbulence coefficient on jet performance is multifaceted; an increase in the turbulence coefficient accelerates the decay of axial velocity and diminishes jet penetration depth. Enhanced turbulence also results in a more uniform velocity distribution across the jet's cross-section, thereby reducing the velocity gradient. Maximum jet range is curtailed as the turbulence coefficient rises, attributed to the accelerated energy dissipation and mixing, which prompt the jet to lose momentum at a faster rate (Abramovich, 1963). Regarding droplet dispersion, an elevated turbulence coefficient intensifies lateral spray spread yet diminishes droplet penetration in the longitudinal direction. Consequently, in applications where a greater jet range is desired, it is advisable to use a lower exit turbulence coefficient.

From Eq. (6), the free submerged jet range is inversely proportional to the turbulence coefficient. For a specific fan, adding rectification and reducing wall roughness are feasible ways to increase the jet range.

2.4 Effect of Air Duct Geometric Structure

The fan duct structure critically impacts the performance of the induced jet by optimizing flow characteristics and regulating exit velocity. Key factors include duct shape, dimensions, length-to-diameter ratio, internal roughness, and contraction/expansion structures. These elements influence fluid resistance, turbulence, energy loss, and jet uniformity. Additionally, components like bends and flanges introduce local resistance and turbulence, affecting the jet structure. Collectively, these factors enhance shear effects and droplet breakup, thereby improving the overall performance and efficiency of the induced jet.

From the perspective of the macroscopic dimensions of the fan duct, the jet range of the fan is primarily influenced by the duct length (L) and the diameter (D) of the duct exit (Eq. 6). A longer duct dissipates more mechanical energy due to resistance along its length. However, sufficient duct length is essential to mitigate velocity disparities at the jet outlet cross-section. Concerning duct diameter, a larger D leads to a higher value of jet range (s) in Eq. (6). The relationship between s and D assumes a constant fan output power (W_a) and equates the fan diameter to the duct diameter. In actual projection systems, W_a varies under different operational conditions, influenced by energy losses within the duct.

When the fan's performance curve (relating fan outlet pressure to air volume flow rate) is available, the precise air jet range can be determined by identifying the intersection point between the fan performance curve and the system pressure loss curve (Eq. (10), derived from Eq.(1), Fig. 2). Adjusting parameters like duct geometry, friction factor, and turbulence coefficient optimizes the fan's power utilization based on Fig. 2. Without knowledge of the fan's performance curve, inserting the rated output power into Eq. (10) might result in a marginally larger calculated jet range compared to observed values.

$$\Delta P_{loss} = \frac{1}{2}\xi_0 \rho u_0^{\ 2} + \frac{1}{2}\frac{L}{D}\lambda \rho u_0^{\ 2} = \left(\xi_0 + \frac{L}{D}\lambda\right)\frac{8\rho}{\pi^2 D^4}Q^2 \qquad (10)$$

3. VERIFICATION OF THE THEORE-TICAL MODEL

Equation (6) reflects the relationship between the free jet range, fan parameters, and duct structure. To validate the accuracy of this empirical formula, the paper conducts experimental verification using circular air jets produced by a small fan.

3.1 Small-Scale Experiment Setup

The schematic diagram of the experimental setup is illustrated in Fig. 3, featuring a small mixed flow fan, sheet light source, hot wire anemometer, camera, and other equipment. The subsequent section will provide a detailed introduction to the device and instrument parameters used in the experiment.

The small-scale fan experiment was conducted with performance parameters listed in Table 4. The fan model used in the experiment is the Shengshida frequency conversion mixed flow fan SE-A100.

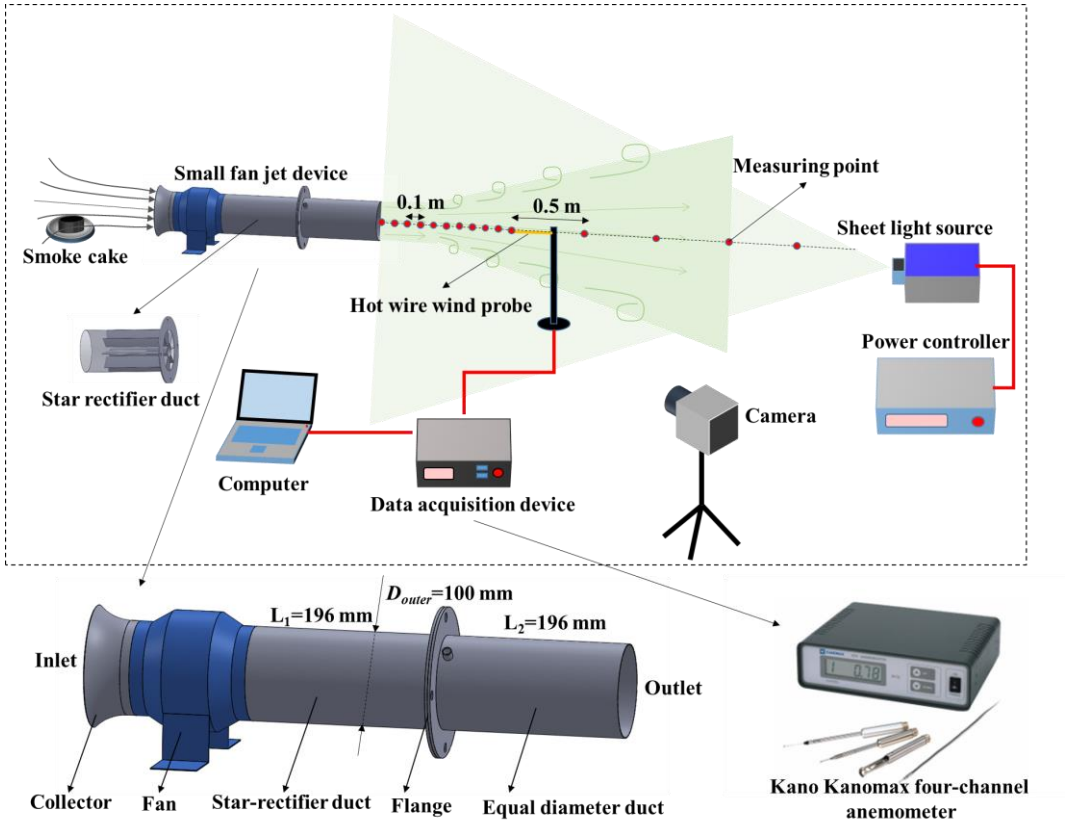

Fig. 3 Schematic diagram of the overall experimental setup

Table 4 Performance Parameters of the mixed-flow fan

Fan parameters	Value
Maximum power	18 W
Maximum flow rate	275 m^3/h
Maximum pressure	334 Pa
Frequency	50/60 Hz
Rotate speed	5000 RPM
Outer diameter of outlet	100 mm
Inner diameter of outlet	98 mm
Voltage	220 V

Based on the size of the fan, the duct illustrated in Fig. 3 was built with an air inlet located on the left side. A collector was integrated to minimize turbulence in the inlet flow. A rectifier section was included at the fan outlet to satisfy the aspect ratio of L_1/D=2, with a star rectifier duct positioned in this section. Additionally, a straight duct was attached at the duct outlet to rectify the flow and fulfill the L_2/D=2 requirement.

A Kano Kanomax four-channel anemometer, model KA12, was utilized to measure the air velocity (Fig. 3) (Fernandez et al., 2007, 2011). This advanced anemometer allows for the simultaneous connection of four probes to the main unit, enabling simultaneous air velocity measurement at four distinct points. Equipped with an RS232C analog output port, it can seamlessly interface with computers, printers, and various control systems. The device boasts a wide measuring range of 0–50 m/s, offering a display resolution of 0.01 m/s for velocities up to 9.99 m/s and 0.1 m/s for higher speeds. Operating at a sampling frequency of 10 Hz, a single

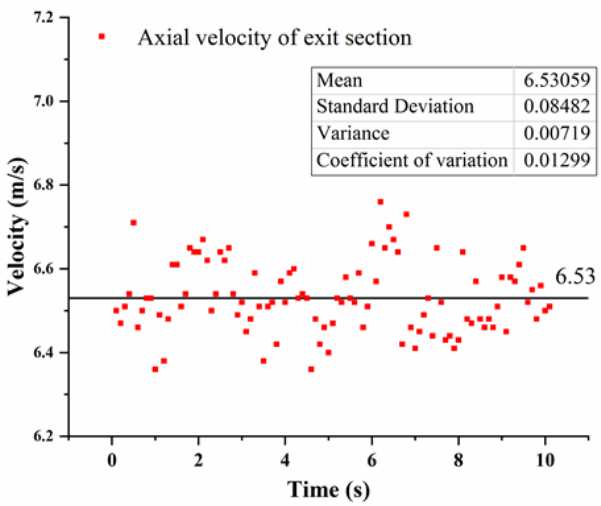

Fig. 4 Data collected using a hot-wire anemometer in 10 s

sample was taken over a duration of 10 s. Figure 4 presents the sampling process undertaken using the hot wire anemometer during a test. Notably, the maximum fluctuation in air velocity recorded was 3.5%, signifying that the stability of the fan's flow field exceeds an impressive 95%. Consequently, leveraging the free turbulent jet generated by this fan for experimental validation purposes is considered viable.

In addition to the Kano Kanomax anemometer (Kanomax Japan Incorporated), other measuring equipment

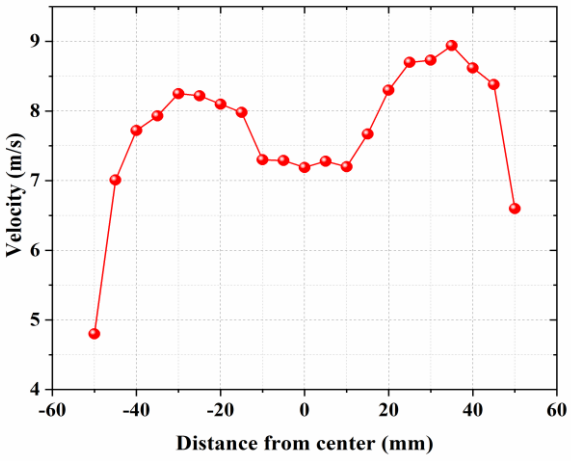

Fig. 5 Velocity distribution of fan outlet cross-section

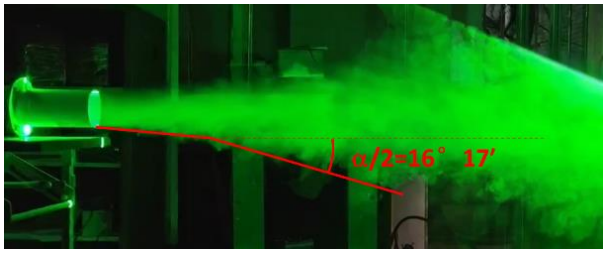

Fig. 6 Smoke tracer diagram of fan jet

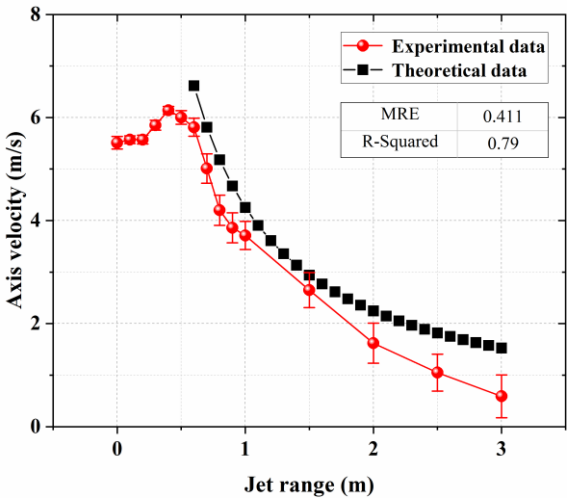

Fig. 7 Fan jet axial velocity curves and theoretical curves of empirical formulas in the main region

used included the manometer model EY-200A and the Pitot tube. The manometer has a measurement range of 0 to ±999 Pa with a resolution of 0.1 Pa, making it suitable for measuring positive, negative, and differential pressures of gases within its specified range. By connecting a Pitot tube to the manometer, air velocity can also be accurately measured.

Furthermore, the diffusion angle of the fan jet was initially determined through the smoke observation method. This involved lighting a smoke cake at the fan's inlet to generate smoke, allowing for the visualization of the flow field. A sheet light source was used for imaging purposes, providing a clear view of the smoke patterns and aiding in the precise diffusion angle measurement.

3.2 Comparison Between Experimental and Theoretical Results

Initially, the Pitot tube was used to approximate the fan outlet velocity at around 9 m/s, resulting in a Reynolds number (*Re*) of approximately 60369.6. By utilizing Eq. (7), the viscous sublayer thickness was 2.198×10^{-4} m. The pipeline experiments involved the use of both inner and outer polished pipes, with the internal surface roughness specified as *Ra* 0.8. Given that the roughness is smaller than the viscous sublayer thickness, the pipes can be classified as belonging to the hydrodynamic smooth pipe. According to the Blasius formula, the Darcy friction factor along the pipe was 0.02.

To gain further insights into the flow characteristics, the velocity distribution at the exit section of the fan's rectifying duct and the axial velocity distribution of the external wind field were measured using a hot-wire anemometer. Figure. 5 illustrates the radial velocity distribution at the fan outlet cross-section, showing higher velocities towards the edges compared to the central region. This discrepancy can be attributed to the rotational movement of the fan blades, inducing a radial velocity component in the airflow. While the blades in the rectifier attempted to mitigate this radial velocity, some components persisted, leading to the observed velocity distribution pattern. This phenomenon is consistent with the findings of Louw et al. (2014), who reported similar velocity distribution patterns in their study on axial flow fans operating at low flow rates. Louw et al. observed that at low flow rates, the downstream fan jet shifts more diagonally outward, and reverse flow occurs between the fan jet and the rotational axis. This behavior is due to the interaction between the fan's rotational flow and the duct geometry, which introduces additional complexity into the flow field. The study by Louw et al. (2014) provides empirical evidence supporting the velocity distribution observed in Fig. 5, thereby validating the results.

The visualization of the flow field at the fan outlet indicates a measured diffusion angle (α) of approximately 33° (Fig. 6). Utilizing Eq. 9, the turbulence coefficient at the fan outlet section was estimated to be around 0.106. Comparing this value to the data in Table 3, where the turbulence coefficient for an axial fan with a guide plate is listed as approximately 0.12, a relatively small difference is observed. Given the minor difference between these two values, we ultimately decided to use 0.12 for our calculations. This discrepancy can be attributed to the pronounced turbulence observed at the edge of the fan jet, leading to an unclear jet boundary. As a result, the actual measured jet diffusion angle tends to be smaller than expected, impacting the calculated turbulence coefficient and deviating from the values typically associated with fan configurations featuring guide plates.

In Fig. 7, the measured axial velocity downstream of the duct outlet is compared to the predicted velocity distribution as per Eq. (4), and the error bars represent the standard deviation of the measured values. It is noted in Section 2.4 that due to the lack of a performance curve provided by the manufacturer, the actual output power of

the fan is slightly lower than the rated output power. Consequently, the measured velocity tends to be marginally lower than the predicted values. However, the overall trends in variation between the theoretical and experimental curves are in agreement. The mean relative error (MRE) between the theoretical and experimental curves is 0.411, with a goodness-of-fit (R-squared) value of 0.79. This level of reliability aligns with our expectations.

To further verify the theoretical model, a full-scale experiment will be conducted in Section 5.1. This experimental validation process will provide additional insight and confirmation regarding the accuracy and applicability of the theoretical model in practical scenarios.

3.3 Uncertainty Analysis

It is necessary to analyze the errors in experimental measurements. The total error in an experimental measurement is commonly represented by two components: a fixed (bias) error and a random (precision) error. The precision error is determined by taking N repeated measurements from the parameter population, whose characteristics can be approximated by the precision index (S), which is defined in Equation (11) (Abernethy et al., 1985; Moffat, 1985, 1988), where $\overline{X}$ denotes the average value of X.

$$S=\left[\frac{\sum_{k=1}^{N}\left(X_k-\overline{X}\right)^2}{N-1}\right]^{1/2} \tag{11}$$

The bias error is the systematic error that is considered to remain constant during a given test. Thus, the 95 percent confidence uncertainty (U) is calculated by Eq. (12).

$$U=\left(B^2+S_{\overline{X}}\right)^{1/2} \tag{12}$$

Based on the data, we estimate the velocity error in our small-scale experiment as follows: precision error (S_{us}) ≈ 0.01 m/s from Fig. 5 measurements and bias error (B_{us}) ≈ 0.02 m/s, considering the hot-wire anemometer and other systematics. Therefore, the total velocity error (U_{us}) is ≈ ±0.02 m/s.

4. DESIGN OF LONG PROJECTION WATER MIST SYSTEM

We have developed a long-range axial-flow induced spray device specifically tailored for addressing transformer fire incidents (Eq. (6)). Given the substantial quantity of oil stored within the transformer body and conservator, the potential firepower can reach up to 200 MW. In such high-energy situations, there is a risk of bushing or transformer body explosions that could render traditional water mist systems surrounding the transformer ineffective.

To address this challenge, the development of a long-range water mist projection system becomes imperative. The goal is to enable the extinguishing of transformer fires from a distance. Given the extensive heat release from the fire source, the water mist projection range must extend beyond 30 m, while ensuring a sufficiently high-water mist spray density to effectively combat the flames. This approach aims to enhance firefighting capabilities and mitigate the impact of large-scale transformer fires with substantial heat and energy output.

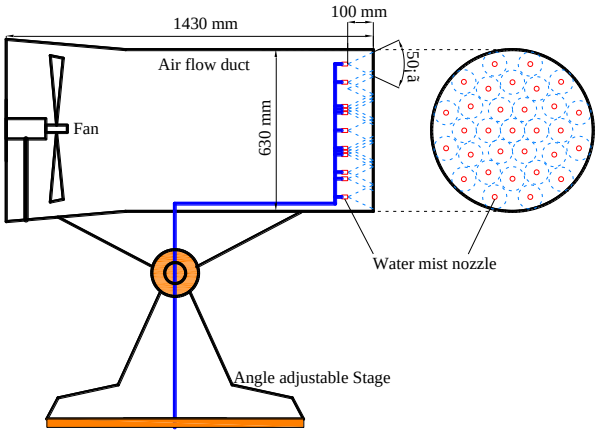

Fig. 8. Nozzle arrangement in the duct

4.1 Arrangement of Water Mist Nozzles

For an 800 kV converter transformer shielded by three firewalls, the maximum area covered by the oil flow is estimated to be 184 m². Referring to the technical standards outlined in the Chinese specification for water mist fire extinguishing systems (GB 50898-2013, 2015), the water mist spray density required for fully submerging an oil fire in a converter transformer must exceed 2 L/(m²·min). Consequently, the total water flow rate needed should surpass 368 L/min. Considering factors such as obstruction from the transformer body and potential droplet loss during long-range travel, a total water flow rate of 720 L/min was designated for the water mist projection device.

To meet the specified water consumption rate, 31 water mist nozzles were installed near the duct outlet, each featuring four orifices, a spray angle of 50°, and a constant of 13.4 (K=13.4). When the nozzle inlet pressure was set at 3 MPa, the total water flow rate achieved by the water mist projection device reached 719.5 L/min. The $D_{v0.99}$ (droplet size where 99% of the volume is made up of smaller droplets) of the water mist remained below 400 mm at a spray range of 1 m. To ensure the even distribution of water mist droplets across the duct's cross-sectional area and prevent droplet coalescence, the nozzle positions were carefully arranged as depicted in Fig. 8.

Given the 50° spray angle and the nozzles being positioned 100 mm away from the duct outlet, it was determined that the duct diameter should be a minimum of 630 mm to accommodate the water mist projection system effectively. By adhering to these design specifications, the water mist projection device was optimized to efficiently combat transformer fires by projecting a fine water mist over a wide area while maintaining desired water flow rates and droplet sizes.

4.2 Fan Selection and Outlet Diameter of the Duct

To guarantee the projection range of the fire-fighting device is sufficiently long, s value should be higher than 20 m. According to Eq. (3), when we set x = 30 m, u_m = 2.5 m/s (conservative projection), D = 630 mm, L = 2D,

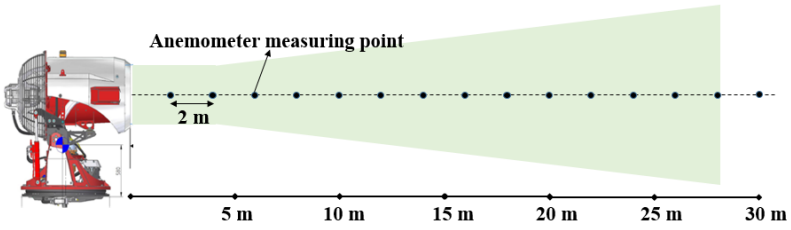

Fig. 9 Measurement positions along the duct axis

a = 0.12, we can get u_0 = 30.53 m/s. Following Eq. (1) with these parameters, we can determine the fan dynamic pressure (P_v) and the fan static pressure loss (P_s). Since u_0 = 30.53 m/s, D = 630 mm, air Viscosity = 1.81×10^{-05} Pa·s, air density = 1.21 kg/m^3, Reynolds number at the duct outlet is 1.30×10^6, taking the roughness ε = 0.50 mm calculates to get λ_{theory}= 0.02. The local loss coefficient ξ is conservatively estimated to be 0.5 to account for factors like the presence of rectifier structures and flanges in the duct. Taking into consideration the energy loss in the fan, the fan's output power should exceed 8264.71 W, which is calculated based on the total power required for the airflow. Since additional energy loss can occur due to the nozzles and pipelines affecting the axial airflow, a turbofan with an input power of 12500 W was chosen to ensure sufficient energy for the airflow.

It is important to acknowledge that the actual output power of the fan and the air jet range may slightly differ from the calculated values, especially if the performance curve of the fan is not precisely known. Therefore, selecting a fan with slightly higher power than the calculated requirement helps account for uncertainties and ensures effective operation of the fire-fighting system.

5. PERFORMANCE OF THE FULL-SCALE LONG PROJECTION WATER MIST SYSTEM

5.1 Wind Velocity Distribution Along the Axis Downstream of the Duct

To meet the requirements for extinguishing transformer fires, a long-range water mist system was developed. The system includes a turbofan installed at the duct inlet, water mist nozzles at the outlet, and the duct mounted on an angle-adjustable stage (Fig. 9). This versatile device can be installed in a fixed position, on firefighting robots, or on firefighting vehicles, offering flexibility and adaptability in various firefighting scenarios. Key specifications of the turbofan are detailed in Table 5.

To assess the airflow range, a portable electronic anemometer, with measurement error of 2%, was employed to measure the axial velocity distribution along the duct axis in the absence of water mist. The measurement points are indicated in Fig. 9. The data was collected at an ambient temperature of 20°C, with an air density of 1.21 kg/m^3, and an air viscosity of 1.81×10^{-5} Pa·s.

Based on the calculations using the parameters in Table 5, the Reynolds number was determined to be

Table 5 Key parameters of the projection device

Parameters	Value
Duct length (m)	1.48
Outlet diameter D (m)	0.63
Duct cross-sectional area (m^2)	0.311725
Raged flow rate (m^3/s)	11.84553
Input power (W)	12500
Internal efficiency η_0	0.8
Mechanical efficiency η_1	0.96
Roughness ε (mm)	0.25-0.5

Table 6 Characteristic parameters of the turbine-fan

Parameters	Value
Output power, W_a (W)	9600
Reynolds number, Re	1.64×10^6
The viscous sublayer, δ (m)	7.86×10^{-5}
Darcy friction factor, λ	0.0186
Turbulence coefficient, a	0.09

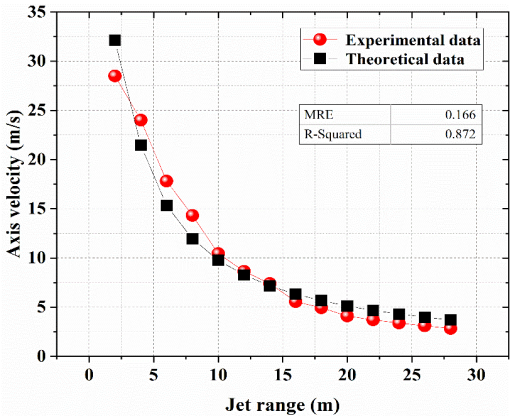

Fig. 10Axial velocity of the turbine-fan and the theoretical curve

1.64×10^6. Considering Table 2 and Fig. 2, the theoretical value of λ_{theory} was calculated to be 0.0186 when the duct wall roughness ε=0.50 mm. The projection device utilizes a turbofan as the induction source with a circular outlet, which is treated as a circular nozzle with guide vanes. Based on Table 3, the outlet turbulence coefficient was estimated to be 0.09.

Subsequently, key airflow parameters in the duct were predicted and presented in Table 6. The theoretical axial air velocity distribution was then computed and compared with the measured axial air velocity distribution in Fig. 10, which exhibits the same behavior as the velocity

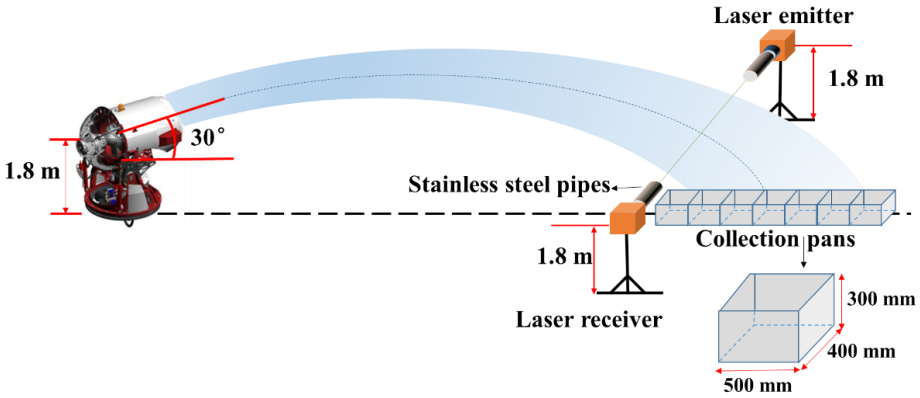

Fig. 11 Schematic diagram of the test device for droplet size and range

distribution of submerged water jets measured in a large-scale tank by Lee et al. (2008). At a distance of 25 m, the axial velocity exceeds 2 m/s, indicating that the turbofan's performance meets the firefighting requirements. The MRE between the theoretical and experimental curves was 0.166, with an R-squared value of 0.872. These results suggest a strong agreement between the experimental data and the empirical formula (Eq. 4), affirming the feasibility of using Eq. (6) to predict the airflow range of the real-scale projection device.

Similarly, the velocity measurement error for large-scale experiments needs to be considered. The precision error (S_{ul}) was approximately 2% of the maximum measured value of 0.6 m/s, while the bias error (B_{ul}) was approximately 0.5 m/s. Therefore, the total error (U_{ul}) in the velocity measurement for large-scale experiments is approximately ±0.8 m/s.

5.2 Projection Range, Density, and Droplet Size of the Spray

According to the relevant standards (GB 19156-2019; GB 7956-2014), the water mist spray range was defined as the horizontal distance from the outlet of the injection device to the center of the water mist falling point on the flat ground. The elevation angle of the injection device was set to 30 degrees, with the environmental wind having a velocity less than 2 m/s in the same direction as the spray. The falling point was determined through water mist density measurement.

To measure the water mist density on the ground, collection pans sized 400 × 500 × 300 mm were positioned along the injection direction on the flat ground (Fig. 11). Due to the initial unsteadiness of the water mist spray, collection was conducted for both 30 s and 90 s. By subtracting the water volume collected at 30 s from that at 90 s, the water volume collected during the steady 60-s spraying stage was determined. The spray density was then calculated based on the spray time, collected water volume, and pan area, with the measurement being repeated three times. The position with the highest spray density was considered the falling point of the water mist.

Water pressure was maintained at 3 MPa throughout the experiment. The results indicated that the spray range of the projection device measured 30.2 m, slightly surpassing the airflow range. This implies that the axial airflow substantially enhanced the water mist spray range. At the falling point, the water mist density was recorded at 43.2 L/(min•m^2), markedly exceeding the required value of 2 L/(min•m^2). This suggests that water droplet sedimentation during transport is within acceptable limits.

Due to droplet coalescence, breakup, and sedimentation, the droplet size of water mist undergoes major variations during long-range transport. To evaluate its efficacy in fire suppression, we measured droplet size at the point where the water spray falls. Utilizing a Winner 2000 laser particle size analysis system positioned at the falling point, our testing setup, shown in Fig. 11, included a projection device center elevated at 1.8 m and an injection device set at a 30° elevation angle. The laser source and photoelectric detector of the particle size analyzer were carefully aligned and positioned at 1.8 m above the ground.

Given the extensive cross-sectional area of the water mist spray, accurately measuring droplet size presented challenges. To address this, we strategically placed two stainless steel pipes with an 8 cm diameter in front of the laser emitter and receiver to obstruct droplets near the measurement zone (spanning a 40 cm laser path). Moreover, due to the high water density at the falling point, waterproof membranes were used to shield the electronic device components during testing.

The results of the tests indicated that at a spray range of 30 m, the droplet sizes measured were $D_{v0.5}$ = 362 □m and $D_{v0.97}$ = 573 m. These findings suggest that the droplet size of the water mist at this range is conducive to rapidly absorbing heat, smoke, and harmful gases within the affected area in the event of an accident.

5.3 Suppression Effect of a Full-Scale 800 Kv Transformer Fire

To verify the performance of the proposed device, a fire extinguishing experiment of a full-scale ±800 kV converter transformer was conducted. The transformer body dimensions were 8757 mm (length), 4752 mm (width), and 4942 mm (height). To simulate real conditions, three firewalls were erected around the transformer, each measuring 9 m in height and 400 mm in thickness. Injection devices were strategically positioned on the extended lines of the north and south side firewalls. The injection devices were set at a height of 9 m and a horizontal distance of 26.5 m from the valve hall side wall.

To replicate a severe fire scenario, oil pans were placed on the entire oil sump and the top of the transformer

Table 7 Comparison of axial flow-induced spray technology with existing technologies

Technology	Range (m)	Flow rate (L/min)	Cost	Advantages	Limitations
Axial flow-induced spray	30-50	200-700	Middle	Long-range coverage, smoke elimination, water-efficient, environmentally friendly	Dependent on stable power supply
Water Mist (Wang, 2019)	＜5	＜10	Low	Water-saving and efficient, no impact hazard, high safety	Limited to small indoor fires, extremely short range, unable to address open environments or large-scale fires
Fire Monitor	30-100	100-1000	Middle	Long-range, flexible flow rate, suitable for suppressing localized fire points, simple and easy-to-maintain equipment	Extremely high water usage, strong water flow impact can damage equipment/buildings, point-to-point fire-fighting, weak coverage for large-scale fires
Turbine Fire Truck (Wesierski, 2023)	20-70	1800	High	Ultra-high flow rate for rapid fire suppression, suitable for high-risk scenarios	Bulky, extremely high energy and noise levels, hazardous (high-temperature exhaust), deployment restricted (requires flat terrain)

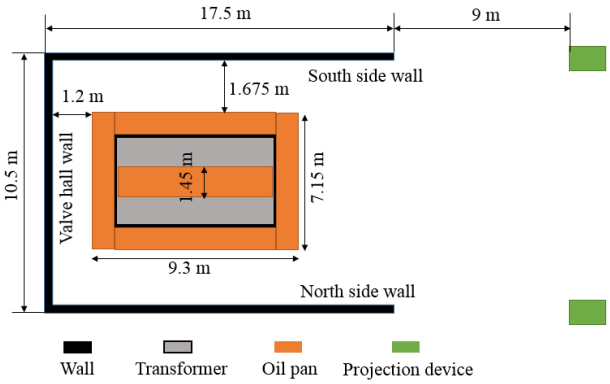

Fig. 12. Arrangement of the full-scale fire extinguishing experiment

body. The oil pans had a thickness of 10 cm and covered a total area of 51.1 m^2. By employing a heat release rate calculation model for rectangular pool fires, the total heat release rate from the oil pans was estimated to be between 81.31 and 124.56 MW.

During the experiment, transformer oil at 70°C was continuously supplied to the transformer tank at a flow rate of 150 L/min, leading to oil overflow from the top of the transformer. Additionally, two nozzles were installed on the bushing to simulate an oil spray fire, with each nozzle having a flow rate of 0.15 kg/s. Detailed sizes and configurations within the fire space are depicted in Fig. 12.

Figure 13 illustrates the oil-fire-burning state of the large-scale transformer and the firefighting operations following the activation of the projection devices. In this scenario, the pool fire had a 3-min pre-combustion time, with oil overflow commencing simultaneously. The oil spray was initiated at 7 min, and the projection devices were activated at 11 min.

The combustion of the transformer oil generated a substantial amount of heat and produced notable black smoke (Fig. 13(a)). By manipulating the spray angle, the water mist sprays were effectively dispersed to cover all fire-affected areas surrounding the transformer. Flame and smoke vanished where water mist was applied (Fig. 13(b)). After 3 min of continuous water mist spraying, the fire was successfully extinguished (Fig. 13(c)). Owing to its long projection range, high water mist density, and small droplet size, the proposed device can effectively handle extensive accident areas from a considerable distance.

5.4 Comparative Analysis with Existing Technologies

Based on the above findings of the axial flow-induced spray device, we compared and analyzed its performance parameters with those of traditional water mist technology, fire monitor technology, and turbine fire truck technology, as well as their respective advantages and limitations (Table 7).

The comparative analysis demonstrates that axial flow-induced spray technology offers major advantages in long-range fire suppression with efficient water usage and smoke elimination capabilities. While it requires a stable power supply and has limitations in extremely long-range applications, it provides a versatile and environmentally friendly solution for a wide range of fire scenarios. Further, axial flow-induced spray technology offers a major advantage in its versatility. Beyond fire suppression, it can be adapted for agricultural irrigation, industrial cooling, coal mine dust control, and environmental protection by adjusting parameters like flow rate and fan performance. This adaptability highlights its high potential and broad applicability across multiple fields. Future research will focus on enhancing the adaptability of this technology to further expand its application scope.

6. CONCLUSIONS

A semi-empirical model was developed by integrating fluid mechanics theory, classical jet theory, and the dimensions of air duct structures to describe the velocity distribution and range of free-submerged jets. This model explains how various parameters, including the Darcy friction factor, turbulence coefficient, and

(a) (b) (c)

Fig. 13 Oil-fire experiment of full-size transformer: (a) Fully developed fire before projection devices were turned on; (b) spray after 1 min free burning; and (c) fire extinguished 3 min after spray projection

dimensional characteristics of the air duct, affect the jet's water projection range. The effectiveness of the model has been validated through both small-scale and full-scale experimental testing, offering invaluable insights for the design of remote spray equipment.

Furthermore, a water mist projection device was refitted and tested, surpassing the projection range of a pure air jet. Operating with a fan power of 12500 W and a water pressure of 3 MPa, the device achieved an effective projection range of approximately 30 m. At a distance of 30.2 m, the water mist density was measured at 43.2 L/(min•m^2), with droplet sizes of $D_{v0.5}$ at 362 mm, $D_{v0.97}$ at 573 mm, and droplet velocities exceeding 3.5 m/s. When two of these devices were utilized, they successfully extinguished a large-scale 800 kV transformer fire with a heat release rate ranging from 81.31 to 124.56 MW in 3 min, while also effectively suppressing smoke generation during the firefighting operation.

The accuracy of empirical models in predicting axial velocity decay of single-phase air jets has been demonstrated through experiments, but extensive errors still exist in predicting the structure of axial-induced spray jet flows. Due to the higher density and momentum of spray jets compared to pure air jets, the range of spray jets is notably greater than that of pure air jets. Therefore, subsequent research will combine the theory of floating jet flows to establish the equations of motion for composite flows, further exploring the relationship between the range of axial-induced spray jets, the structure of the duct, and the initial characteristics of the jets.

ACKNOWLEDGEMENT

The authors would like to acknowledge the Key Project of Anhui Province Science and Technology Breakthrough Plan (No. 202423l10050018) and the National Natural Science Foundation of China (52404260).

CONFLICT OF INTEREST

The authors declare that they have no known competing financial interests or personal relationships that could have appeared to influence the work reported in this paper.

AUTHORS CONTRIBUTION

Huazhong Sun: Formal analysis; Writing - Original draft; Co-first author: **Xiaolong Zhu:** Writing - Review & Editing; Supervision; **Zhigang Wang:** Experimental Equipment/Venue; **Jiangyue Zhao:** Data Curation; **Shi Hu:** Validation; **Chaohang Xu:** Methodology; Corresponding author **Xishi Wang:** Writing - Review & Editing; Project administration; Funding acquisition;

REFERENCES

Abdulrahman, S. A., Chetehouna, K., Cablé, A., Skreiberg, Ø., & Kadoche, M. (2021). A review on fire suppression by fire sprinklers. *Journal of Fire Science*, *39*(6), 512-551. https://doi.org/10.1177/07349041211013698.

Abernethy, R. B., Benedict, R. P., & Dowdell, R. B. (1985). ASME measurement uncertainty. *ASME Journal of Fluids Engineering*, *107*(2), 161-164. https://doi.org/10.1115/1.3242450.

Abramovich, G. N. (1963). *The theory of turbulent jets*. MIT Press.

Albertson, M. L., Dai, Y., Jensen, R., & Rouse, H. (1950). Diffusion of submerged jets. *Transactions of the American Society of Civil Engineers*, *115*(1), 639-664. https://doi.org/10.1061/TACEAT.0006302.

Baturin, B. B., & Liu, Y. N. (1965). *Principle of Industrial Ventilation*. China Industry Press.

Bressler, H., Rammoser, D., Neumaier, H., & Terres, F. (1996). Experimental and predictive investigation of a closed coupled catalyst converter with pulsating flow. *SAE Technical Paper,* 960564.

https://doi.org/10.4271/960564.

Cao, X. Y., Ren, J. J., Bi, M. S., Zhou, Y. H., & Li, Y. M. (2017). Experimental research on the characteristics of methane/air explosion affected by ultrafine water mist. *Journal of Hazardous Materials*, *324*, 489-497. https://doi.org/10.1016/ j.jhazmat.2016.11.017.

Chen, H. S., Liang, X. Z., Tan, Q. C., & Kang, S. (2000). Experimental study at the exit flow field of an axial flow fan with variable setting angle. *Journal of China Coal Society*, *25*, 412-415. (in Chinese).

Colebrook, C. F. (1939). Turbulent flow in pipes, with particular reference to the transition region between the smooth and rough pipe laws. *Journal of the Institution of Civil Engineers*, *11*(4), 133-156. https://doi.org/10.1680/IJOTI.1939.13150.

Collin, A., Boulet, P., Parent, G., & Lacroix, D. (2007). Numerical simulation of a water spray—radiation attenuation related to spray dynamics. *International Journal of Thermal Sciences*, *46*(9), 856-868. https://doi.org/10.1016/j.ijthermalsci.2006.11.005.

Daugherty, R. L., Franzini, J. B., & Finnemore, E. J. (1985). *Fluid mechanics with engineering applications*. Eighth edition.

Del Taglia, C., Blum, L., Gass, J., Ventikos, Y., & Poulikakos, D. (2004). Numerical and experimental investigation of an annular jet flow with large blockage. *ASME Journal of Fluids Engineering*, *126*(3), 375-384. https://doi.org/10.1115/1.1760533.

Fernández Oro, J. M., Argüelles Díaz, K. M., Santolaria Morros, C., & Blanco Marigorta, E. (2007). Unsteady flow and wake transport in a low-speed axial fan with inlet guide vanes. *ASME Journal of Fluid Engineering*, *129*, 1015-1029. https://doi.org/10.1115/1.2746920.

Fernández Oro, J. M., Argüelles Díaz, K. M., Santolaria Morros, C., & Galdo Vega, M. (2011). Numerical simulation of the unsteady stator-rotor interaction in a low-speed axial fan including experimental validation. International *Journal of Numerical Methods in Heat and Fluid Flow*, *21*, 168-197. https://doi.org/10.1108/09615531111105380.

FM Approvals. (2016). *Approval standard for water mist systems.* FM global technologies LLC, Norwood, MA, Edition 5560.

GB 19156-2019. (2019). *Technical code for fire monitor*. China. (in Chinese).

GB 50898-2013. (2015). *Technical code for water mist fire extinguishing system*. China. (in Chinese).

GB 7956-2014. (2014). *Technical code for fire fighting Vehicles*. China. (in Chinese).

Gieras, M. (2008). Flame acceleration due to water droplets action. *Journal of Loss Prevention in the Process Industries*, *21*(4), 472-477. https://doi.org/10.1016/j.jlp.2008.03.004.

Görtler, H. (1942). Berechnung von aufgaben der freien turbulenz auf grund eines neuen näherungsansatzes. *Zeitschrift für angewandte Mathematik und Mechanik*, *22*, 244-254. https://doi.org/10.1002/zamm.19420220503.

Haiwainet. (2020, August 5). Beirut Explosion Leaves at Least 78 Dead and 4,000 Injured, Mayor Weeps in Interview. Haiwainet News. http://news.haiwainet.cn/n/2020/0805/c3541093-31849508.html (Accessed December 2, 2024).

Hotz, C., Haas, M., Wachter, S., Fleck, S., & Kolb, T. (2021). Two-phase free jet model of an atmospheric entrained flow gasifier. *Fuel*, *304*, 121392. https://doi.org/10.1016/j.fuel.2021.121392.

Hussein, H. J., Capp, S. P., & George, W. K. (1994). Velocity measurements in a high-Reynolds number, momentum-conserving, axisymmetric, turbulent jet. *Journal of Fluid Mechanics*, *258*, 31-75. https://doi.org/10.1017/S002211209400323X.

JB/T 9728-2014. (2014). Ministry of industry and information technology of the people's republic of china. (in Chinese).

Jenft, A., Collin, A., Boulet, P., Pianet, G., Breton, A., & Muller, A. (2014). Experimental and numerical study of pool fire suppression using water mist. *Fire Safety Journal*, 67, 1-12. https://doi.org/10.1016/j.firesaf.2014.05.003.

Lakehal, A., Aksouh, M. & Medelfef, A. (2025). Numerical study of the compressible air flow through a two-output fluidic oscillator. *Journal of Applied Fluid Mechanics, 18*(4), 880-891. https://doi.rog/10.47176/jafm.18.4.3128

Lee, S. Y., Dimenna, R. A., Leishear, R. A., & Stefanko, D. B. (2008). Analysis of turbulent mixing jets in a large scale tank. *ASME Journal of Fluids Engineering*, *130*(1), 011104. https://doi.org/10.1115/1.2820989.

Li, C. X., Li, X. Y., Li, P. M., & Ye, X. M. (2014). Numerical investigation of impeller trimming effect on performance of an axial flow fan. *Energy*, 75, 534-548. https://doi.org/10.1016/j.energy.2014.08.015.

Li, G. C., Pan, C. Y., Liu, Y. P., Zhu, X. L., Ni, X. M., Zhao, X. D., Chen, G. X., & Wang, X. S. (2021). Evaluation of the effect of water mist on propane/air mixture deflagration: Large-scale test. *Process Safety and Environmental Protection*, *147*, 1101-1109. https://doi.org/10.1016/j.psep.2021.01.034.

Liu, X., Liu, J., Wang, D., & Zhao, L. (2021). Experimental and numerical simulation investigations of an axial flow fan performance in high-altitude environments. *Energy*, *234*, 121281. https://doi.org/10.1016/j.energy.2021.121281.

Liu, Y. P., Wang, X. S., Zhu, P., Li, G. C., Ni, X. M., & Zhang, J. (2019). Experimental study on gas jet suppressed by water mist: a clean control technique in natural gas leakage incidents. *Journal of Cleaner Production*, *223*, 163-175. https://doi.org/10.1016/j.jclepro.2019.03.107.

Louw, F. G., von Backström, T. W., & van der Spuy, S. J.

(2014). *Investigation of the flow field in the vicinity of an axial flow fan during low flow rates.* Proceedings of the ASME Turbo Expo 2014: Turbine Technical Conference and Exposition (Vol. 1A: Aircraft Engine; Fans and Blowers). Düsseldorf, Germany. https://doi.org/10.1115/GT2014-25927.

Luo, M. G., & Li, J. X. (2013). Technical innovation of new turbojet seven fire engine. *Fire Technology and Product Information*, *8*, 56-59. (in Chinese).

Lv, D., Tan, W., Zhu, G., & Liu, L. (2019). gasoline fire extinguishing by 0.7 mpa water mist with multicomponent additives driven by CO2. *Process Safety and Environmental Protection*, *129*, 168-175. https://doi.org/10.1016/j.psep.2019.07.002.

Mawhinney, J. R., Dlugogorski, B. Z., & Kim, A. K. (1994). *A closer look at the extinguishing properties of water mist.* Proceedings of the International Association for Fire Safety Science (IAFSS) Conference (Vol. 4, pp. 47-60). Ottawa, Canada.

Ministry of machinery industry, fourth academy, spray painting ventilation simulation test group (1976) Diffusion Angle of Jet from Circular Duct Outlet. *Journal of Architectural Technology Communications (Heating, Ventilation, and Air Conditioning)*. (04), 24-28+35. https://doi.org/10.19991/j.hvac1971.1976.04.004.

Moffat, R. J. (1985). Using uncertainty analysis in the planning of an experiment. *ASME Journal of Fluids Engineering*, *107*(2), 173-178. https://doi.org/10.1115/1.3242452.

Moffat, R. J. (1988). Describing the uncertainties in experimental results. *Experimental Thermal and Fluid Science*, *1*(1), 3-17. https://doi.org/10.1016/0894-1777(88)90043-X.

Moody, L. F. (1944). Friction factors for pipe flow. *Transactions of the American Society of Mechanical Engineers*, *66*(8), 671-678. https://doi.org/10.1115/1.4018140

Panchapakesan, N. R., & Lumley, J. L. (1993). Turbulence measurements in axisymmetric jets of air and helium. Part 1. Air jet. *Journal of Fluid Mechanics*, *246*, 197-223. https://doi.org/10.1017/S0022112093000096.

Rajaratnam, N., & Subramanya, K. (1967). Plane turbulent free jet and wall jet. *Journal of the Royal Aeronautical Society*, *71*(680), 585-587. https://doi.org/10.1017/S000192400005507X.

Santangelo, P. E., Jacobs, B. C., Ren, N., Sheffel, J. A., Corn, M. L., & Marshall, A. W. (2014). Suppression effectiveness of water-mist sprays on accelerated wood-crib fires. *Fire Safety Journal*, *70*, 98-111. https://doi.org/10.1016/j.firesaf.2014.08.012.

Santangelo, P. E., Tarozzi, L., & Tartarini, P. (2016). Full-scale experiments of fire control and suppression in enclosed car parks: a comparison between sprinkler and water-mist systems. *Fire Technology*, *52*, 1369-1407. https://doi.org/10.1007/s10694-016-0569-3.

Schlichting, H. (1960). *Boundary Layer Theory*. McGraw Hill Book Company, Inc.

Tollmien, W. (1926). Berechnung turbulenter Ausbreitungsvorgänge. *Zeitschrift für angewandte Mathematik und Mechanik*, *6*, 468-478. https://doi.org/10.1002/zamm.19260060604.

Wang, X. S. (2019). *Water Mist*. Science Press, Beijing, China.

Wang, X. S., Kong, X. X., & Zhu, P. (2016). *An axial flow induced spray device.* China Patent CN201610210880.4.

Welten, H., Bressler, H., & Rammoser, D. (1993). Optimisation of catalytic converter gas flow distribution by CFD prediction. *SAE Technical Paper,* 930780. https://doi.org/10.4271/930780.

Węsierski, T. (2023). Study of the extent and degree of water and heavy foam coverage of streams generated by a firefighting vehicle equipped with an SO3 Jet engine. *Fire Safety Journal*, *140*, 103870. https://doi.org/10.1016/j.firesaf.2023.103870.

Wu, L., & Wang, J. (2021). *Experimental study of flow characteristics in round jet flow using particle image velocimetry (PIV).* Proceedings of the 2021 28th International Conference on Nuclear Engineering. Volume 2: Nuclear Fuels, Research, and Fuel Cycle; Nuclear Codes and Standards; Thermal-Hydraulics. V002T07A018. ASME. https://doi.org/10.1115/ICONE28-64534.

Xinhua News Agency. (2015, August 15). UAV Team Aerial Photos of the '8·12' Accident Site in Tianjin Port. Government of China News. https://www.gov.cn/xinwen/201508/15/content_2913392.htm (Accessed December 2, 2024).

Xu, H. L., Wang, X. S., Li, Y., Zhu, P., Cong, H. Y., & Qin, W. X. (2017). Experimental investigation of methane/coal dust explosion under influence of obstacles and ultrafine water mist. *Journal of Loss Prevention in the Process Industries*, *49*, 929-937. https://doi.org/10.1016/j.jlp.2017.04.016.

Ye, X., Ding, X., Zhang, J., & Li, C. (2017). Numerical simulation of pressure pulsation and transient flow field in an axial flow fan. *Energy*, *129*, 185-200. https://doi.org/10.1016/j.energy.2017.04.076.

Zhang, F. C., Zirwes, T., Wachter, S., et al. (2023). Numerical simulations of air-assisted primary atomization at different air-to-liquid injection angles. *International Journal of Multiphase Flow*, *158*, 104304. https://doi.org/10.1016/j.ijmultiphaseflow.2022.104304.

Zhu, X. L., Chen, G., Wang, Z. G., Wu, L. S., Luo, J. F., & Wang, X. S. (2022). Extinguishment of a transformer fire with a long projection water mist system. *Fire Safety Journal*, *130*, 103603. https://doi.org/10.1016/j.firesaf.2022.103603